Powder Technology xxx (2016) xxx-xxx

Contents lists available at ScienceDirect

Powder Technology

journal homepage: www.elsevier.com

New hybrid CPU-GPU solver for CFD-DEM simulation of fluidized beds

H.R. Norouzi, R. Zarghami *, N. Mostoufi

School of Chemical Engineering, College of Engineering, University of Tehran, 11155/4563 Tehran, Iran

ARTICLE INFO

Article history:
Received 29 April 2016
Received in revised form 29 October 2016
Accepted 29 November 2016
Available online xxx

Keywords:
Parallelization
Graphical processing unit (GPU)
OpenFOAM
Fluidized bed
CFD-DEM

ABSTRACT

The algorithm and implementation details of a new parallel CFD-DEM solver that uses both CPU and GPU resources for computations are presented in this study. The new solver supports complex geometries, various shapes of mesh, converges at very high fluid velocities and executes with available computational resources of a simple desktop computer. At first, verification studies were performed for the solver. Among three parts of the solver, the DEM solver and coupling solver results were verified bysimple problems for which analytical solutions exist . Then, the solver results were evaluated in three cases of gas-solid flows with various geometries (from simple to complex) and various numbers of particles. For a large system that contains 870 k particles, it took around 6 h (with two CPU cores) to complete each second of simulation while in a smaller system with 47 k particles, it took only 30 min (with one CPU core). Results obtained by the new solver were compared with experimental data. The solver can properly predict the frequency of bubble passage and intensity/share of macrostructures in the bubbling regime, while underestimates intensity/share of meso-structures. The hydrodynamics of a spouted bed with draft tube was well-captured in terms of the fountain shape and its maximum height, particle concentration profile in different parts and time-averaged upward velocity of particles. The solver was also used to investigate the particle dynamics in a Wurster bed. Two velocity profiles were tested. In the first velocity profile, an unstable fountain with slugging conveying in the draft tube was observed while in the second velocity profile, a stable fountain withdispersed conveying in the draft tube. This was found to be attributed to the formation of the bubbles in the annulus region.

1. Introduction

Fluidized and spouted beds have many applications in chemical industries, ranging from polymerization reactors and combustors to coaters, granulators and dryers. In the past decades, the understanding about these contactors has been increased, mainly via experiments. This helped to find new applications for them, tune and control their operations, design and scale-up, optimize and troubleshoot of the process. However, sometimes a deep understanding of inter- and intra-phase interactions at small length scales requires sophisticated models which can describe the motion of phases with desired details. Various modeling with different length scales have been developed and used for describing multiphase flows in fluidized beds and spouted beds [1]. Among them, the two fluid model (TFM) and combined computation fluid dynamics/discrete element method (CFD-DEM) are the most used ones. In the TFM, both phases are considered as interpenetrating continua. In the CFD-DEM model, which is the main focus of the present work, the fluid phase is considered as continuum and the solid phase as discrete particles.

Since the first introduction of CFD-DEM, it has been developing in three distinct fields: theoretical developments, new applications and numerical implementation. In the theoretical development field, new force-displacement and friction laws for mechanical contacts [2–7], closure laws for various fluid-particle interactions [8–15] and coupling methods [16,17] have been proposed. On the other hand, researchers have added various sub-models to the core model and coupled it with heat and mass transfer equations to apply it to new applications, such as fluid-particle flow of cohesive particles [18–21], reacting multiphase flows [22–24] and flows with heat transfer [25–27]. However, a CFD-DEM simulation is computationally very intensive which restricts its use to lab-scale simulations with short durations. Therefore, the efficient and robust numerical implantation of the CFD-DEM is crucial for achieving advancements in the field of multiphase modeling.

The governing equations of CFD-DEM should be implemented into a numerical code with the following properties: it should be executed fast, should be robust and can be used to systems with general/complex geometry. Using efficient numerical algorithms for various steps of calculations and parallelization are the two main solutions to have a fast code. A robust code should handle large number of particles and support the full range of phase porosities (from packed bed to dilute phase), the full range of superficial gas velocity (from packed bed to bubbling, turbulent and fast fluidizations) and polydispersity of particles. In addition, it should support common shapes of fluidized beds with rectangular and circular cross-sections or with conical base (like spotted beds).

The main focus of this article is developing a new solver for simulating fluid-solid flow in fluidized beds that has the abovementioned properties. As mentioned before, the main limitation of the CFD-DEM is the high computational demand which makes parallelization necessary. The calculations related to solving the governing equations of the fluid phase can be efficiently parallelized using space decomposition method using the message passing interphase (MPI) on the distributed-memory basis, while the DEM calculations (due to its

* Corresponding author.
Email address: rzarghami@ut.ac.ir (R. Zarghami)

http://dx.doi.org/10.1016/j.powtec.2016.11.061
0032-5910/

low granularity) is better to be parallelized using loop-level parallelization on the shared-memory basis. We were aiming to perform large simulations with reasonable execution time on simple computer desktops. Today, desktop computers have multi-core processors as well as a graphical processing unit (GPU). This provides a huge computation resource that makes is possible to perform teraflops calculations. With this in mind, we used a combination of CPU and GPU to speed-up the execution of CFD-DEM code. OpenFOAM® (an open source parallel CFD package parallelized using MPI) was used for solving the fluid phase equations (it uses CPU resources). Implementation of the DEM was through the CUDA platform (it uses GPU resources). Moreover, calculation of the coupling parameters was also parallelized using MPI. The numerical implementation of different parts of this solver is first given in detail followed by the verification and validation of the solver results and evaluation of its performance in a bubbling fluidized bed, a flat bottom spouted bed and a Wurster fluid bed.

2. Model

2.1. Fluid phase equations

For the fluid phase motion, the volume-averaged Navier-Stokes equations for linear momentum conservation and continuity equation for mass conservation are used. In formulation of these equations, all variables are assumed to be locally averaged over each control volume of the simulation domain. Size of the control volume is chosen large enough to allow averaging over quantities and small enough to capture the main characteristics of the flow. This is mostly chosen at least 3 to 4 times larger than the size of particles. The continuity and momentum conservation equations are as follows [28]:

$$\frac{\partial\left(\rho_f\varepsilon_f\right)}{\partial t}+\nabla.\left(\rho_f\varepsilon_f\vec{u}\right)=0 \tag{1}$$

$$\frac{\partial\left(\rho_f\varepsilon_f\vec{u}\right)}{\partial t}+\nabla.\left(\rho_f\varepsilon_f\vec{u}\vec{u}\right)=-\varepsilon_f\nabla p-\varepsilon_f\nabla.\vec{\tau}_f-\overrightarrow{F}^{f-p}+\rho_f\varepsilon_f\vec{g} \tag{2}$$

where t is time, ρ_f is the density of fluid, $\vec{u}$ is the local velocity vector fluid, p is the fluid pressure and $\vec{\tau}_f$ is the shear stress tensor. ε_f and $\overrightarrow{F}^{f-p}$ are the local fluid volume fraction and the local volumetric momentum transfer between fluid and particles, referred as coupling parameters for the fluid phase equations. The shear stress tensor has two contributions as follows:

$$\vec{\tau}_f=\vec{\tau}^{v}+\vec{\tau}^{t} \tag{3}$$

where $\vec{\tau}^{v}$ is the viscous stress tensor obtained from the following equation for an incompressible fluid with μ_f as the dynamic viscosity of the fluid:

$$\vec{\tau}^{v}=-\mu_f\left(\nabla\vec{u}+\left(\nabla\vec{u}\right)'\right) \tag{4}$$

and $\vec{\tau}^{t}$ is the turbulent stress tensor that should be calculated based on the applied turbulent model in the simulation. In the present implementation, the $k-\varepsilon$ turbulent model was used. The turbulent model used by Zhou et al. [29] was adopted here. The transport equations for the turbulent kinetic energy and dissipation rate of turbulent kinetic energy are given by:

$$\frac{\partial}{\partial t}\left(\varepsilon_f\rho_f k\right)+\nabla.\left(\vec{u}\varepsilon_f\rho_f k\right)=\nabla.\left(\varepsilon_f\left(\mu_f+\frac{\mu_t}{\sigma_k}\right)\nabla k\right)+G_f-C_D\varepsilon_f\rho_f\varepsilon \tag{5}$$

$$\frac{\partial}{\partial t}\left(\varepsilon_f\rho_f\varepsilon\right)+\nabla.\left(\vec{u}\varepsilon_f\rho_f\varepsilon\right)=\nabla.\left(\varepsilon_f\left(\mu_f+\frac{\mu_t}{\sigma_\varepsilon}\right)\nabla\varepsilon\right)+\frac{\varepsilon}{k}\left(C_1G_f-C_2\varepsilon_f\rho_f\varepsilon\right) \tag{6}$$

where

$$\mu_t=C_\mu\rho_f k^2/\varepsilon \tag{7}$$

$$G_f=\mu_t\varepsilon_f\nabla\vec{u}\left(\nabla\vec{u}+\left(\nabla\vec{u}\right)'\right) \tag{8}$$

where k and ε are the turbulent kinetic energy and dissipation rate of turbulent kinetic energy, and μ_t is the turbulent viscosity. Other constants in this closure turbulent model are $C_\mu = 0.09$; $C_D = 1.0$; $\sigma_k = 1.0$; $\sigma_\varepsilon = 1.3$; $C_1 = 1.44$ and $C_2 = 1.92$ [29].

2.2. Discrete element method

In the DEM, individual particles constitute the solid phase. The motions of particles (linear and angular) are tracked in time by applying force and torque balance equations, referred to as Newton's and Euler's second laws of motion, respectively. The most common formulation of the DEM is soft-sphere in which the particles are allowed to have small (compared to the size of particles) overlaps. The mechanical force acting on particles is calculated based on these overlaps using force-displacement relations. Equations of motion for a spherical particle are:

$$m_i\frac{d\vec{v}_i}{dt}=m_i\frac{d^2\vec{x}_i}{dt^2}=\sum_{j\in CL_i}\vec{f}_{ij}^{\,p-p}+\vec{f}_i^{\,f-p}+m_i\vec{g} \tag{9}$$

$$I_i\frac{d\vec{\omega}_i}{dt}=\sum_{j\in CL_i}\left(\overrightarrow{M}_{ij}^{t}+\overrightarrow{M}_{ij}^{r}\right) \tag{10}$$

where m_i, I_i, $\vec{v}_i$, $\vec{\omega}_i$ and $\vec{x}_i$ are the mass, the moment of inertia, the linear and the angular velocities and the center position of particle i, respectively. $\overrightarrow{f}_{ij}^{\,p-p}$ is the particle-particle or the particle-wall interaction force (here, only the mechanical contact force) and $\vec{f}_i^{\,f-p}$ is the force exerted on particle from the fluid surrounding the particle. $\overrightarrow{M}_{ij}^{t}$ and $\overrightarrow{M}_{ij}^{r}$ are the tangential torque and rolling friction torque between particle pairs or a particle and a wall. For evaluating the contact force, the nonlinear model proposed by Tsuji et al. [30] for normal direction and Di-Renzo and Di Maio [7] for tangential direction and for the rolling friction torque, the model proposed by Zhou et al. [31] were used. In the above equations, the summation is performed on

particles which are in the contact list of particle, CL_i. This list is constructed based on the spatial position of particles in every time step of the simulation. Determination of the contact lists of particles requires efficient algorithms to minimize/reduce the computational effort of this step. This will be discussed in the following sections.

2.3. Coupling parameters

In the CFD-DEM modeling, the fluid phase equations are formulated based on the Eulerian approach, which are discretized over a stationary grid mesh (spatial) and time, while the particle phase equations are formulated based on the Lagrangian approach, which are discretized over time. The spatial resolution of the fluid properties/field variables is as large as the mesh size while the spatial resolution of the particle variables is the size of particles which is much smaller than the mesh size. These two spatial resolutions do not coincide and hence interphase coupling in CFD-DEM requires special attention. Interphase coupling parameters are the fluid volume fraction, the volumetric momentum exchange and fluid-particle interaction force on particles. The fluid particle interaction force is calculated as:

$$\overrightarrow{f}_i^{f-p} = \overrightarrow{f}_i^{d} + \overrightarrow{f}_i^{\nabla p} + \overrightarrow{f}_i^{\nabla.\vec{\tau}_f} + \overrightarrow{f}_i^{r} \tag{11}$$

where $\overrightarrow{f}_i^{d}$ is the drag force exerted on particle, $\overrightarrow{f}_i^{\nabla p} = -V_i \nabla p$ is the pressure gradient force on particle, $\overrightarrow{f}_i^{\nabla.\vec{\tau}f} = -V_i\left(\nabla.\vec{\tau}_f\right)$ is the force due to change in the shear stress around the particle and $\overrightarrow{f}_i^{r}$ includes other remaining interactions, like lift force. The volumetric interphase momentum exchange in each fluid cell with the volume of V_{cell} is calculated by:

$$\overrightarrow{F}^{f-p} = \frac{1}{V_{cell}} \sum_{i=1}^{k_v} \left(\overrightarrow{f}_i^{d} + \overrightarrow{f}_i^{r}\right) \tag{12}$$

where k_v is the number of particles whose centers are in that fluid cell. Many correlations have been proposed for calculating the drag force exerted on particles, form conventional correlation like Ergun-Wen & Yu [32–34] and Di Felice [15] to new correlations proposed by Hill et al. [10], Benyahia et al. [8], Beetstra et al. [11] and Cello et al. [13]. Here, the correlation proposed by Beetstra et al. [11] was used:

$$\begin{aligned}\overrightarrow{f}_i^{d} &= 3\pi\mu_f\varepsilon_f d_i\left(\vec{u}-\vec{v}_i\right)\left\{\left(\frac{180\varepsilon_p}{18\varepsilon_f^2}\right)+\varepsilon_f^2\left(1+1.5\sqrt{\varepsilon_p}\right)\right.\\ &\left.+\left(\frac{0.413}{24\varepsilon_f^2}\right)\left(\frac{\varepsilon_f^{-1}+3\varepsilon_p\varepsilon_f+8.4Re_i^{-0.343}}{1+10^{3\varepsilon_p}Re_i^{-(1+4\varepsilon_p)/2}}\right)Re_i\right\}.\end{aligned} \tag{13}$$

where d_i is the particle diameter, $\varepsilon_p = 1 - \varepsilon_f$ is the solid volume fraction and Re_i is the particle Reynolds number:

$$Re_i = \frac{\rho_f\varepsilon_f d_i\left|\vec{u}-\vec{v}_i\right|}{u_f}. \tag{14}$$

Other remaining forces are neglected in the present simulations.

The fluid volume fraction in each fluid cell is calculated according to the volume of the particles that occupies the volume of the fluid cell based on the following equation:

$$\varepsilon_f = 1 - \frac{1}{V_{cell}} \sum_{i=1}^{kv} \varphi_i V_i \tag{15}$$

where k_v is the number of particles partially located within the fluid cell and $\varphi_i \in [0, 1]$ denotes the fraction of the volume of particle i that resides in the fluid cell.

3. Implementation details

A CFD-DEM code can be broken down into three parts: DEM solver which solves Eqs. (9) and (10), a CFD solver which solves Eqs. (1) and (2) and the coupling solver which calculates the interphase coupling parameters. A schematic of these solvers, calculation sequence and the data transferred among them are shown in Fig. 1. Each iteration starts with calculating the coupling parameters such as fluid volume fraction, volumetric fluid-particle interactions, etc. These parameters are calculated based on the position and velocity of particles and field variables (pressure and velocity) of the fluid phase in the current time step. Thereafter, in the DEM solver, the iteration loop of DEM starts using the calculated values of $\overrightarrow{f}_i^{f-p}$ and the governing equations of the DEM are solved for Δt_f seconds. The results are new position and velocity of all particles in the next time step. In the CFD solver, using the calculated values of $\overrightarrow{F}_f^{f-p}$ and ε_f, the governing equations of the fluid phase are solved for Δt_f seconds. The results are new field variables of the fluid phase.

3.1. Implementation of DEM solver

The calculations of DEM part are performed on GPU using CUDA® platform. This massively parallel architecture allows performing millions of calculations in parallel on the shared-memory basis. The GPU has its high speed dedicated memory (device memory) for storing the data to be processed on the device. Data transfer between the main memory of CPU (host memory) and the device memory is performed using a gate with a limited speed. Therefore, all the data of DEM should stay on the device memory to avoid data transfer latencies. In this solver, all calculation steps of the DEM part, except saving data to the disk, are performed on GPU. The most computational intensive step of the DEM solver is the contact search between particle pairs and between particle and wall. The parallel algorithm proposed by Mazhar et al. [35] was used for particle-particle contact search. The algorithm is grid-based which is composed of nine steps. In this algorithm, the size of bins is not necessarily equal to or larger than the particles. The algorithm can be used for mono-sized and poly-sized systems. The mapping of particle bounds on the particle grid cell is performed using a parallel radix sort on the array of data which holds bin numbers and particle numbers. After mapping of particles, the local search is performed between particle pairs which are close to each other. Details of this algorithm are presented elsewhere [35].

Another important entity of the DEM solver is the treatment of walls. As a requirement for a general solver, it should be able to simulate containers with arbitrary shape. Triangulation of the wall surface is a logical choice in this regard [28]. By triangulation, the whole surface of the wall is decomposed into plane triangular sub-elements. Then, the contact detection between the wall and particles is

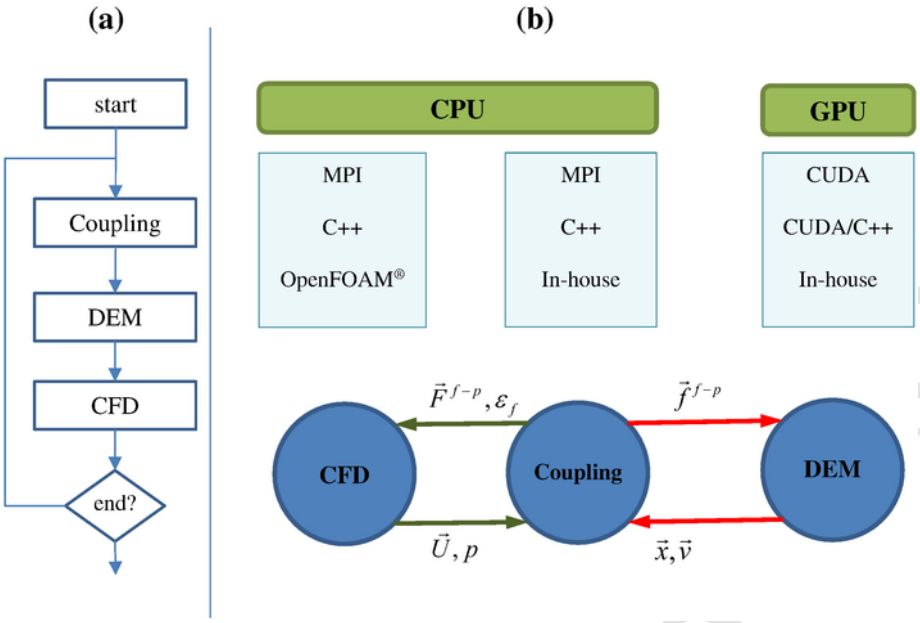

Fig. 1. (a) Schematic of the main solvers of a CFD-DEM code and the iteration loop, (b) different parts of the new solver implemented on CPU and GPU and the data transfer among them.

performed by testing contacts between these sub-elements and particles near them. Fast and robust methods for contact detection between a sphere and triangular sub-element are described elsewhere [36]. In the present work, we have used the so-called barycentric method for particle-wall contact detection [36]. For integrating the linear and rotational equations of motion of particles, the third-orther Adams-Bashforth integration method was used [37].

3.2. Implementation of CFD solver

To solve continuity and Navier-Stokes equations, OpenFOAM® which is an open source code was used [38]. OpenFOAM® discretizes (various schemes from first to higher order) and solves linear partial differential equations (PDEs) using the finite volume method. The code is parallelized using MPI that uses space decomposition for load balancing. The MPI is a distributed memory method which is designed for execution on multiple CPUs.

When dealing with numerical solution of continuity and Navier-Stokes equations, special attention should be paid to two points: the nonlinearity of convective term in Eq. (2) and the pressure-velocity coupling [39] (coupling between momentum and continuity equations). The problem of nonlinearity is solved by linearization of the convective term by considering it as a product of known velocity u^* (either guessed or obtained from previous calculations) and an un-known velocity u. In addition, the pressure field is considered explicit and known, p^*. The resultant linearized equation is solved to obtain the new velocity field. If u^* is true, the resultant velocity field should satisfy the continuity equation. If the continuity equation is not satisfied, the pressure field should be adjusted in a way to eliminate the continuity errors. The Poisson's equation (obtained from continuity equation, see [40] for more details) is solved to obtain the new pressure field.

The linearized momentum equation and Poisson's equation are solved in sequence. Therefore, an algorithm is required to determine how these equations are related and in what sequence they should be solved (coupling). There are various algorithms for coupling these equations, like SIMPLE [41], PISO [42] and PIMPLE. The PISO algorithm is developed for unsteady state problems with small time steps in which the linearized momentum equation is solved once and the pressure is obtained and corrected multiple times. The Courant number in the PISO algorithm should be far less than unity (small time steps for solution) to assure convergence. The SIMPLE algorithm is designed for steady flows wherein the linearized momentum equation is solved once, followed by solution of pressure equation once. To carry the information of the fluid field to the next iteration, relaxation is used for pressure and velocity fields. The SIMPLE algorithm is not very sensitive to the Courant number. The PIMPLE algorithm is a combination of PISO and SIMPLE. It uses both relaxation and multiple pressure corrections. It takes the advantages of both algorithms, i.e., rapid convergence and insensitivity to large Courant numbers.

A new solver based on the PIMPLE algorithm was developed for this code. Details of this solver and discretization of equations can be found elsewhere [40]. It should be noted that the PIMPLE algorithm converges at Courant numbers larger than unity. This is very important for having a stable solver for simulating fluid-particle flows. In some circumstances, the velocity of fluid becomes locally very large (this mostly happens in multiphase flows) and this leads to large local Courant numbers, while it is much smaller than unity in the rest of the domain. If the solver is capable of converging at large Courant numbers, the large errors are not propagated between iterations and it can be safely compensated. Otherwise this large local Courant number may lead to a divergence.

3.3. Implementation of coupling solver

The coupling part of the algorithm was parallelized using MPI (developed in C ++) and all calculations were performed on CPU as shown in Fig. 1b. The coupling part computes the coupling parameters ($\overline{F}^{f-p}, \varepsilon_f$ and $\overline{f}_i^{f-p}$) required by fluid and solid phase equations. Calculation of these parameters needs position and velocity of particles, pressure and velocity fields of fluid (in addition to other properties of these phases). The coupling starts with calling these variables from DEM and CFD parts. Since the DEM variables are stored on the GPU memory, the first processor (processor#0) calls the DEM vari-

ables and distributes particle data to other processors based on the spatial position of particles. In this way, each processor is responsible for calculating a portion of coupling parameters and the computational load is distributed among processors. For mapping particles on fluid cells, available tools in OpenFOAM® were used. OpenFOAM® allows performing a tree-based search over fluid mesh structure and determining the cell that a given point (for example, center of a particle) resides in.

Calculation of the fluid volume fraction was implemented in a way that was not restricted to the type of fluid grid (structured or unstructured) and shape of fluid cell. To this end, the sub-element method [43] was used, in which a spherical particle is divided into N equal parts, each having its own center. For each particle, if the center of any of these sub-elements resides in a fluid cell, the whole volume of that sub-element is assumed to be in that cell. An example of this method of calculating the volume fraction is illustrated schematically in Fig. 2 (shown in 2D for clarity). Number of sub-elements is five in this example. For particle i, the volume of sub-element #5 is not added to the total solid volume in the target fluid cell, but is added to the total solid volume of the adjacent cell. For particle j, volumes of sub-elements #1 and #4 are added to the total solid volume in the target cell and volumes of other sub-elements are added to the total solid volume in the adjacent cells. As mentioned earlier, mapping of these sub-elements onto fluid cells is done by the tools provided in OpenFOAM®. Accuracy of this method increases with increasing the number of divisions. This method is not restricted to the shape of fluid cell, contrary to analytical methods [44] which are developed for specific shape of the fluid cell.

4. Verification and validation

An important step in the development process of a numerical code is the verification and validation of the code results. In verification phase, the code results are compared to the problems whose analytical/exact solution exists. This shows the accuracy of the numerical implementation of the model and shows the probable numerical bugs of the code. However, the verification does not infer the validity of the implemented physical model. The validity of the model is tested using actual experimental data in the operating condition of interest. In this section, we perform verification and validation studies for the implemented code and model.

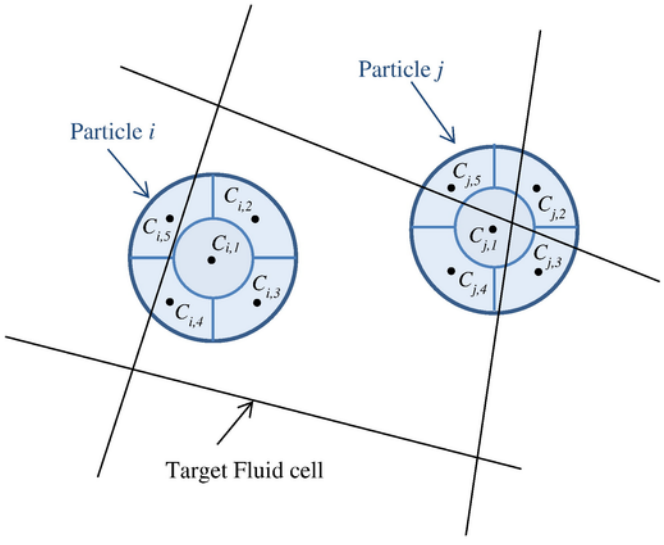

Fig. 2. The sub-element method for calculating the fluid volume fraction.

4.1. Verification

In the verification phase, all components of the code should be tested. The current numerical code contains three main components: DEM solver, CFD solver and coupling solver. The CFD solver is available via OpenFOAM® which has been verified before [45]. Here we perform some verification tests for the DEM and coupling solvers.

4.1.1. Verification of DEM solver

The first set of verification test on the DEM solver was performed on free fall of a smooth particle on a flat wall in the normal direction. This motion consists of three steps: Free fall before contact to the wall, contact with wall and free motion after contact. For a linear visco-elastic contact force model, the analytic expressions for particle center position are expressed as [46]:

$$y(t) = h_0 - \frac{1}{2}gt^2 \tag{16}$$

$$y\left(t - t_{f1}\right) = \left[\frac{g}{\omega_0^2}\cos\left(w\left(t - t_{f1}\right)\right) + \frac{-\sqrt{2g\left(h_0 - r_p\right)} + \frac{\beta g}{\omega_0}}{w}\sin\left(w\left(t - t_{f1}\right)\right)\right]\exp\left(-\beta\omega_0\left(t - t_{f1}\right)\right) + \left(r_p - \frac{g}{\omega_0^2}\right) \tag{17}$$

$$y\left(t - t_{f2}\right) = r_p + v_{f2}\left(t - t_{f2}\right) - \frac{1}{2}g\left(t - t_{f2}\right)^2 \tag{18}$$

$$\beta = \eta_n/2\sqrt{k_n m_i},\quad \omega_0 = \sqrt{k_n/m_i},\quad w = \sqrt{1 - \beta^2\omega_0} \tag{19}$$

where η_n and k_n are damping coefficient and spring stiffness of the linear model in the normal direction. h_0 and y are the initial height and vertical position of the particle center and r_p is the radius of the particle. t_{f1} and t_{f2} are the moments when the first and the second steps are finished and v_{f2} is the velocity of the particle at the end of the second step. The free fall of the smooth particle on a flat wall (normal contact) from the height of 0.1 m was simulated. In these simulations, the coefficient of normal restitution was set at 0.9, 0.7 and 0.5. The particle radius is 1.5 mm, the particle density is 2500 kg/m^3, the normal spring is k_n = 10000 N and the time step for integration is 7.0×10^{-6} s (time step resolution is 20). The accuracy of the results only depends on the type of the integration method and the time step resolution (contact time over integration time step). It was shown that the accuracy of the third order Adams-Bashforth method is less than 1% when the time step resolution is greater than 12 [37]. Here, the time step resolution is 20 which guarantees the accuracy of the numerical integration. The results of the solver were compared with the analytical solution in Fig. 3a. As it can be seen, the DEM solver accurately predicts the particle center position during falling, contact and rebound. The difference between the solver results and exact solution is negligible and cannot be distinguished in this figure. To better measure this difference, the relative absolute error was calculated and the results are shown in Fig. 3b. The error of the DEM solver is below 1% in the whole processes, which is acceptable. The

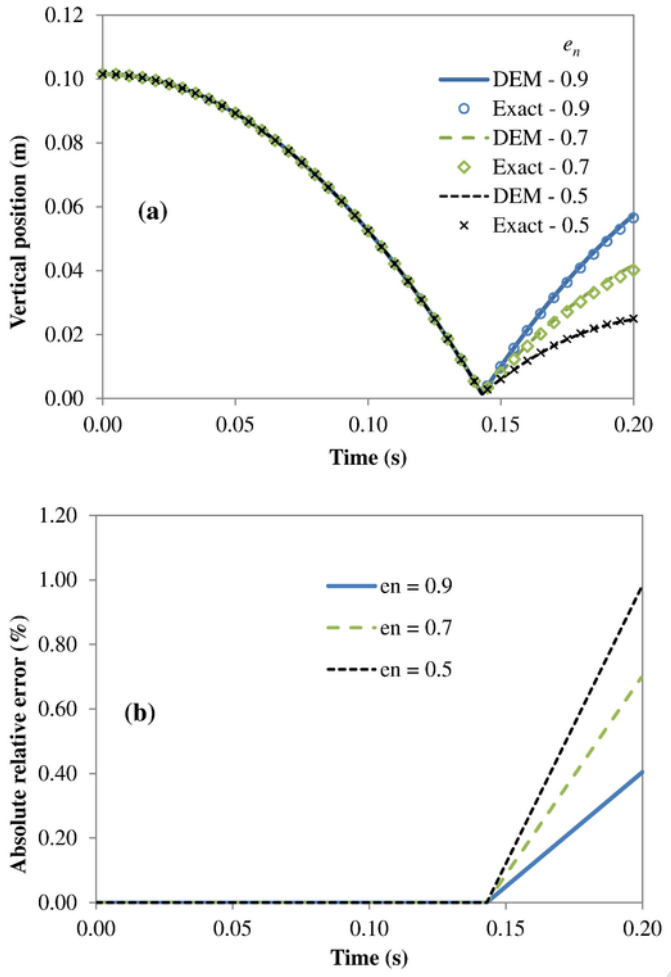

Fig. 3. (a) Evolution of the center position of a sphere during free fall for DEM solver and exact solution and (b) the relative absolute error between the exact and the DEM solver results.

error is zero before the contact since the integrator is of third order and the orders of the equations of motion for both velocity and position of particle are below three. Therefore, the integrator gives the exact solution. However, when particle comes into contact with the wall, some error is introduced in the results. This error is originated from two sources. First, the governing equation of motion for particle in contact with wall is not as simple as that for free falling particle (the analytical solution in Eq. (17) also confirms this). Therefore, the accuracy of the integrator is not enough to exactly find the center position of the particle and a very negligible error is introduced. Second, the nature of DEM integration is discrete and it is possible that the exact moment of the contact is not detected by DEM. This issue has been addressed in [28] in details. It is shown that not detecting the exact moment of contact introduces additional errors in the results.

The simulation results can also be compared to the hard-sphere collision model in a limiting case (normal collision). In each collision of the particle with a flat wall, a fraction of kinetic energy is dissipated into internal energy and the maximum rise height in each rebound of the particle decreases. The relation between the maximum height of particle in n^{th} contact and the initial height of particle is as follows:

$$h_{\max,n} = \left(h_0 - r_P\right) e_n^{2n} + r_P. \tag{20}$$

The results of the simulation were compared to Eq. (20) in Fig. 4a. The maximum height of the particle in each contact with wall is decreased due to the dissipation of kinetic energy and the dissipation rate increases with the coefficient of restitution. The DEM results follow the analytical solution points with minimal errors. The absolute relative errors of the DEM results are also shown in Fig. 4b. The errors are less than 2% in all conditions and decrease as the number of contact increases. As it was mentioned before, the difference between DEM results and the analytical solution is due to the nonlinearity of the equation of motion (when particle and wall are in contact) and the discrete nature of the integration scheme in the solver.

4.1.2. Verification of coupling solver

In the coupling solver, two field variables are calculated: the fluid/solid volume fraction and interphase momentum exchange term. These variables couple the equations of motions of both phases. It is important to verify the numerical implementation of these parts. The terminal velocity test of a very small sphere in the fluid was examined for the verification of the interphase momentum exchange calculation. In an extreme condition, the force balance on a very small sphere in the vertical direction in a medium is governed by [46]:

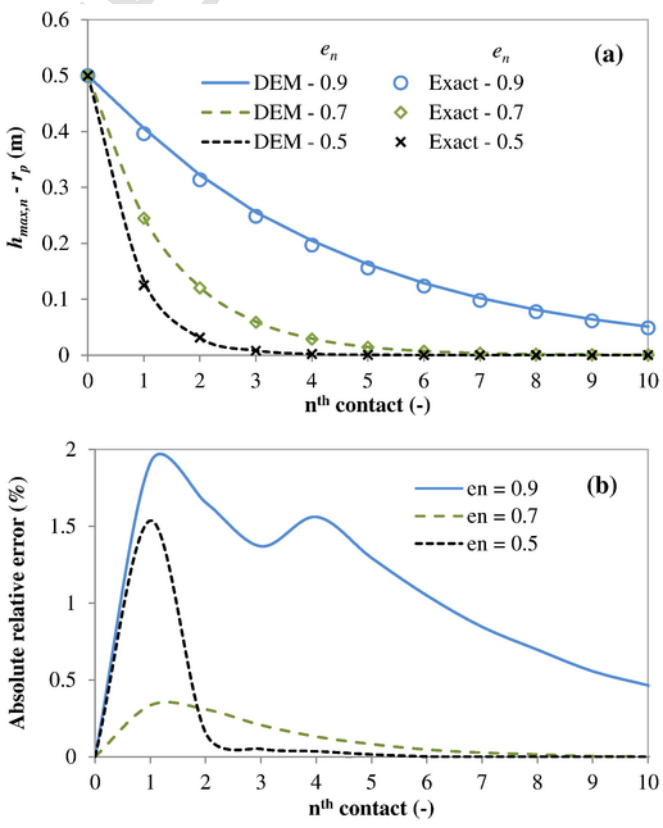

Fig. 4. (a) The maximum height of the particle center in frequent contacts with the flat wall in free fall condition obtained for the DEM solver and the exact solution and (b) the absolute relative error between the DEM solver and the exact solution.

$$\frac{dv_p}{dt} = \frac{3}{4} C_D \frac{\rho_g \left| u_g - v_p \right| \left(u_g - v_p \right)}{d_p \rho_p} - \frac{g\left(\rho_p - \rho_g\right)}{\rho_p} \tag{21}$$

where v_p, ρ_p and d_p are the vertical velocity, density and diameter of the particle and u_g and ρ_g are the velocity and density of the gas. C_D is the drag coefficient exerted on particle and is obtained by [47]:

$$C_D = \frac{24}{\mathrm{Re}} \left(1 + 0.15\mathrm{Re}^{0.687}\right) \tag{22}$$

$$\mathrm{Re} = \frac{\rho_g \left| u_g - v_p \right| d_p}{\mu_g} \tag{23}$$

where μ_g is the viscosity of gas. This equation is valid for Reynolds numbers up to 1000. Eq. (21) was solved by fourth-order Runge-Kutta integration method using the initial condition $v_p(0) = 0$ and the results were considered as the exact solution. Simulations were performed for free falling spheres in a free fluid (in a conduit with the diameter of 0.25 m with free-slip condition on walls) using the CFD-DEM solver. In these simulations, the particle and gas densities were 1000 and 1.2 kg/m^3, gas velocity and gas viscosity were 1 m/s and 1.8×10^{-5} Pa·s, respectively. Two particle sizes of 220 and 250 μm were chosen. The results of the simulations were compared with the exact solution and are illustrated in Fig. 5. As it can be seen, the CFD-DEM solver precisely follows the exact solution. This shows that the CFD-DEM solver can calculate the interphase momentum exchange correctly in this limiting case.

The coupling solver also calculates the solid volume fraction. The procedure of the calculation of this volume fraction in each fluid cell was explained in previous section (sub-element method). It is important to make sure that the whole volume of the particle is considered in the calculation of solid volume fraction using the sub-element method. We formed a packed bed (using the code) with a certain number of particles with known volumes. Then, the volume fraction of the particles in each fluid cell was calculated using the coupling solver. If the solver is correct, the total volume occupied by particles in nonempty fluid cells should be equal to the sum of volume of particles that formed the packed bed. The total solid volume in nonempty cells is obtained by:

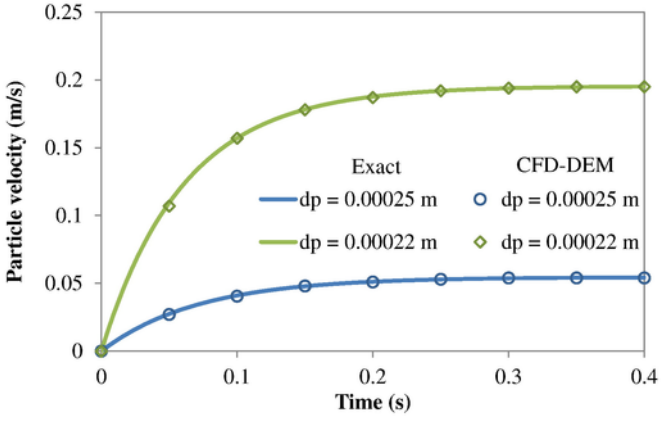

Fig. 5. Evolution of particle velocity in a free fluid obtained from exact solution and CFD-DEM solver.

$$V_{solid} = \sum_{cell} \varepsilon_{p,cell} V_{cell} \tag{24}$$

where $\varepsilon_{p,cell}$ is the volume fraction of solid in the nonempty cell and V_{cell} is the volume of the nonempty cell. The total solid volume obtained from the solver was compared to the sum of the volume of all particles and there was no difference between these two. This shows that the coupling solver does not miss any sub-elements of a particle in the calculation of solid volume fraction.

4.2. Validation and performance

The new solver was evaluated in three fluidized beds with different geometries and operating conditions:

- cylindrical fluidized bed in the bubbling regime.
- flat bottom spouted bed with draft tube and rectangular cross-section.
- wurster fluidized bed, which is used in granulation and coting of particles.

The results of the first and the second simulations were validated with experimental data. All simulations were performed on a desktop computer equipped with an Intel® core™-i7 processor (with 4 3.6-GHz cores) with 12 GB DDR3 RAM, and an NVIDIA GeForce® GTX 660Ti GPU with 2GB DDR5 RAM. The CFD solver was developed on OpenFOAM® v2.4 and it was compiled and tested on Ubuntu® 14.04 operating system. The CPU code was compiled by g ++ v4.8 and GPU code was compiled by the standard CUDA® 7.0.28 compiler.

4.2.1. Bubbling fluidized bed

The time series of pressure fluctuations inside the bubbling fluidized bed was chosen for validating the solver. Pressure fluctuations reflect the dynamics of different flow structures inside the bed at various length-scales (i.e., micro, *meso* and macro). Many studies have shown that pressure fluctuations are a proper indicator of the bed hydrodynamics [48–51]. The experiment was performed in a bed of 15 cm inner diameter and 2 m height. The whole system was electrically grounded to minimize the electrostatic charge effects. This bed was filled with 1500 μm polypropylene particles to the height of 15 cm [52]. Air at the room temperature (25 °C) and atmospheric pressure and velocity of 1.13 m/s (2.5 U_{mf}) was entered the bed through a perforated palate distributor with 1 mm holes arranged in a triangular pitch. A pressure probe (dynamic pressure sensor, type 7261, Kistler, Switzerland) was placed 10 cm above the distributor level and absolute pressure of the bed was recorded with the frequency of 400 Hz.

A simulation with the same operating conditions of the experiment was performed. About 870,000 spherical particles were used in this simulation. Other physical properties and simulation conditions are listed in Table 1. Based on the mesh size and operating conditions, the mean and maximum Courant number were 0.14 and 0.53. To compare the simulation results with the experimental data, the pressure of the gas phase in the simulation was recorded at 10 cm above the distributor with the frequency of 500 Hz. The computational resource of 2 cores (4 logical threads) of the CPU and one GPU was used for this simulation. It took 6 h to complete 1 s of the simulation and it was continued for 20 s.

Fig. 6 shows fluid volume fraction of the bed and velocity of particles at different simulation moments. To see inside of the bed, the whole bed is cut at some parts. Small and large bubbles as well as bubble bursting are evident in this figure. These are characteristics of

Table 1
Physical properties and simulation conditions for bubbling fluidized bed.

Parameter	Value	Parameter	Value
Particles		Bed	
Size (μm)	1500	Diameter/height (m)	0.15/2
Density (kg/m^3)	900	Young modulus (MPa)	10
Young modulus (MPa)	10	Poisson's ratio (−)	0.23
Poisson's ratio (−)	0.23	Dynamic friction (−)	0.3
Dynamic friction (−)	0.3	Rolling friction (−)	0.05
Rolling friction (−)	0.05	Coefficient of restitution (−)	0.8
Coefficient of restitution (−)	0.9		
Air		Simulation	
Density (kg/m^3)	1.2	Time step for fluid (s)	1×10^{-4}
Viscosity (Pa·s)	1.8×10^{-5}	Time step for particle (s)	1×10^{-5}
Velocity (m/s)	1.3	No. of particles (−)	870,000
		No. of CFD cells (−)	84,000
		Mesh shape (−)	Hex
		Mean Courant number (−)	0.14
		Max. Courant number (−)	0.53
		Simulation duration (s)	20

the bubbling regime. The power spectral densities of pressure signals recorded in experiments and simulation are compared with each other in Fig. 7. The frequency range of 0–20 Hz is illustrated in this figure, which corresponds to macro (large bubbles) and *meso* (small bubbles and clusters) structures in the bed. Macro structures occur at frequencies between 0 and 5 Hz and *meso* structures at frequencies from 5 to 20 Hz [49]. It can be seen in this figure that macro structures are more pronounced than *meso* structures in both simulation and experiment. A peak is observed at 3.4 Hz for experiment and at 3.9 Hz for simulation, which are very close to each other. This peak corresponds to the frequency of passage of large bubbles through the bed. This shows that the frequency of bubbles predicted by the model is very close to that of the experiment. Intensities of the spectra are also very close to each other in the macro structure range. However, the model underestimates the intensity of *meso* structures. The underestimation of *meso* structures can be attributed to the turbulent model. The numerical studies show that the k-ε model underestimates the drag force when the Kolmogorov length scale is much smaller than the particle size [53,54]. When the ratio of the particle size to the Kolmogorov length is less than 7, the drag force does not need modifications. However, for larger ratios this drag force requires some modifications as described in [53]. We calculated this ratio based on the simulation results and found that for the majority of the bed (more than 80%) this ratio is lower than 7. However, for the rest of the bed it is greater than 7, which can be a source of the underestimation of *meso* structures. Studying the effect of turbulent model and the corrections to the interphase momentum transfer requires a separate study which is beyond the scope of this study.

4.2.2. *Flat bottom spouted bed*

The next simulation was setup based on the experiments performed by Sutkar et al. [55]. They measured average vertical velocity of particles in a flat bottom spouted bed with a rectangular cross section. The height, width and depth of the bed were 100 cm, 14 cm and 2 cm, respectively. Two flat plates with the length of 32 cm were placed at the middle of the bed and 3 cm above the distributor to form the draft region (see Fig. 8). The bed was initially filled with 1-mm glass beads up to the height of 14 cm. The air entered through the distributor plate with the velocity of 0.32 m/s and a central jet

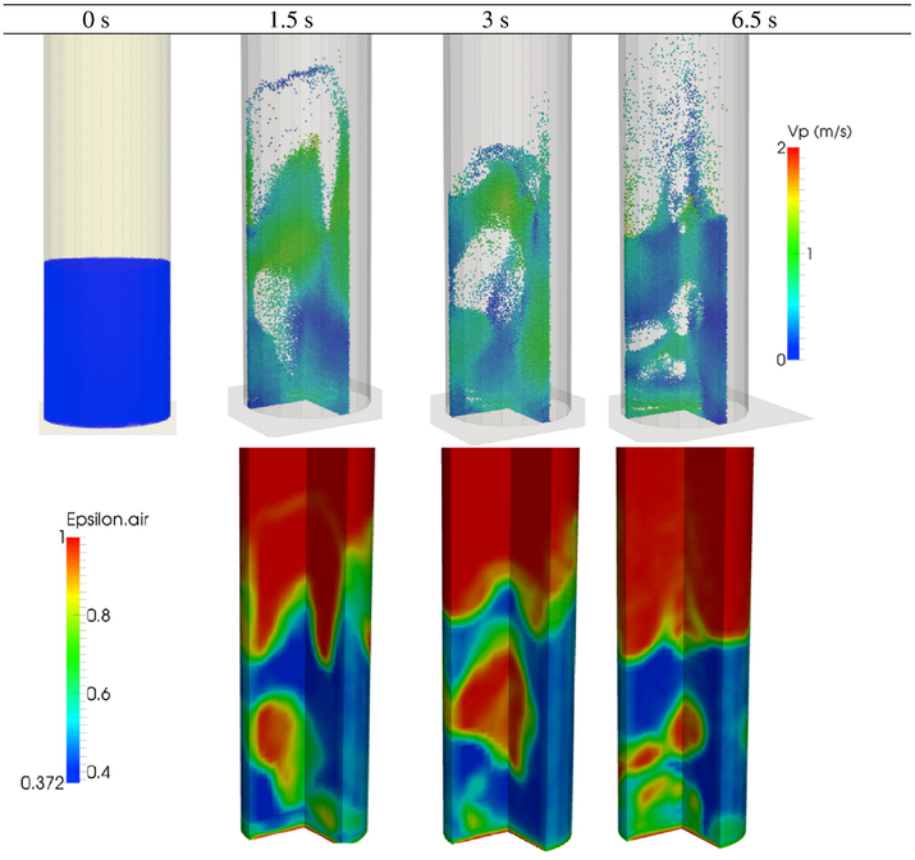

Fig. 6. Snapshots of the bed simulation in bubbling regime at various moments, the top row shows the particles colored based on their velocity magnitude and the bottom row shows the gas volume fraction. Some parts of the bed are cut off to make the inside of the bed visible.

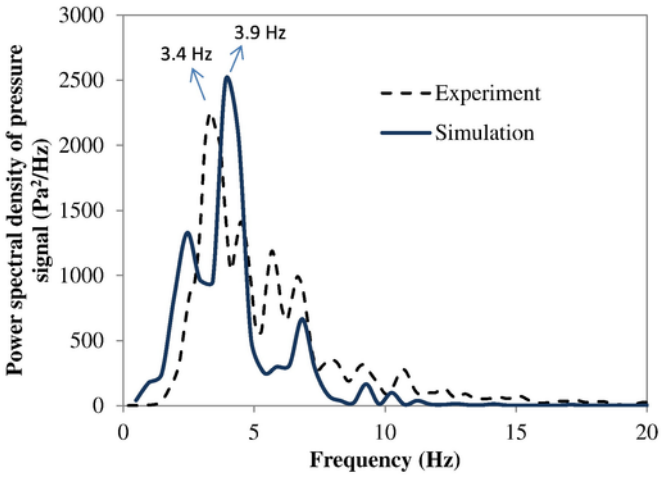

Fig. 7. Power spectral density of pressure signal for the bed in bubbling regime. Pressure signals are measured in an experiment and obtained from a simulation at similar operating conditions.

with the velocity of 28.2 m/s was injected into the bed through a 1-cm-width hole. The simulation was performed for the same geometry and at the same operating conditions. About 460,000 spherical particles were used in the simulation. Physical properties and other simulation data are listed in Table 2. Physical properties of particles related to the contact mechanics are obtained from [55]. According to the operating conditions, mean and maximum Courant numbers were 0.53 and 1.59, respectively, in this simulation. The computational resources were a CPU core (2 logical threads) and a GPU. It took around 6.5 h to complete one second of this simulation and the simulation was performed for 4 s.

Sample snapshots of the simulated bed are compared with experimental results in Fig. 8. As can be seen in this figure, particles near the central jet are accelerated by high gas velocity and rise up in the draft region. A fountain is formed above the draft region where particles are decelerated and deviate gradually to the side walls. Downward continuous flow of particles is formed at two sides of the bed and particles go back to the bottom of the bed through the annulus region. A comparison between experiment and simulation snapshots shows that the model can predict the shape and height of the fountain, high concentration of the particles near the side walls and inside the draft region and the central jet formed bellow the draft region. However, as a noticeable difference, the particles are not evenly distributed between two sides of annulus regions in the experiment while they are evenly distributed in the simulation. As stated by Sutkar et al. [55], this can be attributed to the uneven distribution of particles near the distributor plate (due to the packing condition) before gas injection. This had made the air jet to deviate to the right and lots of particles discharge from this side at the very first moments of the experiment. However, this uneven packing was not the case in the simulation and a straight upward jet was formed form the beginning of gas injection.

For a more precise comparison, the time-averaged vertical velocity of particles in the experiment and the simulation at 30 and 50 cm above the distributor are shown in Fig. 9. According to Fig. 9a the model can well predict the particle velocity in the draft region. However, slight differences can be observed near the walls. This can be attributed to the size of fluid cells that should be at least 3 times larger than the size of particles. With large size of fluid cells, the effect of wall is not very precisely captured and small deviations are observed. Moreover as can be seen in Fig. 9b, a better agreement between the model results and experiment was obtained above the draft region where wall effects are less significant.

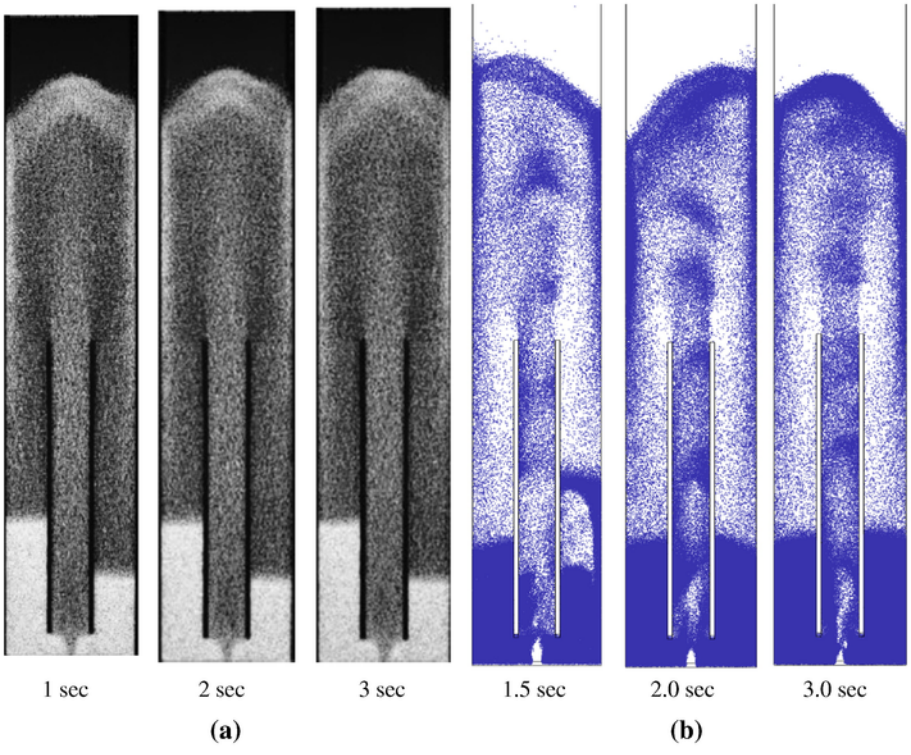

Fig. 8. (a) Snapshots of stable spouting regime in experiment performed by Sutkar et al. [55] and (b) snapshot of the simulation results of the bed with similar operating conditions.

Table 2
Physical properties and simulation conditions for flat bottom spouted bed [55,57].

Parameter	Value	Parameter	Value
Particles		Bed	
Size (μm)	1000	dimensions (m^3)	1 × 0.14 × 0.02
Density (kg/m^3)	2526	Draft tube length (m)	0.3
Young modulus (MPa)	10	Young modulus (MPa)	10
Poisson's ratio (−)	0.23	Poisson's ratio (−)	0.23
Dynamic friction (−)	0.1	Dynamic friction (−)	0.1
Rolling friction (−)	0.05	Rolling friction (−)	0.05
Coefficient of restitution (−)	0.95	Coefficient of restitution (−)	0.95
Air		Simulation	
Density (kg/m^3)	1.2	Time step for fluid (s)	2×10^{-5}
Viscosity (Pa·s)	1.8×10^{-5}	Time step for particle (s)	2×10^{-6}
Velocity (m/s)	0.32	No. of particles (−)	460,000
Jet velocity (m/s)	28.2	No. of CFD cells (−)	67,000
		Mesh shape (−)	Hex
		Mean Courant number (−)	0.53
		Max Courant number (−)	1.59
		Simulation duration (s)	4

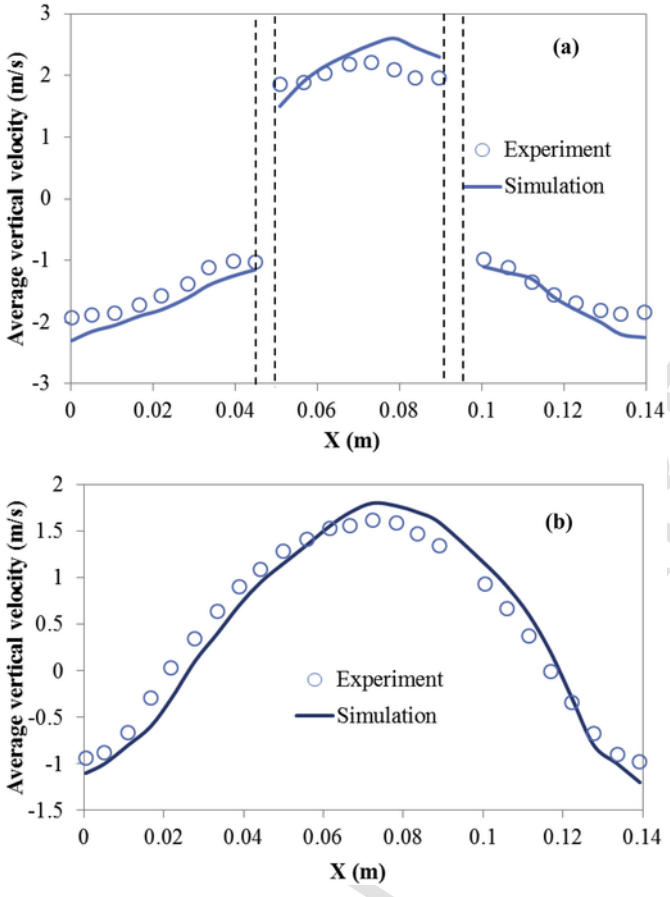

Fig. 9. Time-averaged vertical velocity of particles measured at (a) 30 cm and (b) 50 cm above the distributor. Empty circles shows the experimental data [55] and lines show the simulation results.

4.2.3. Wurster bed

The last set of simulations was performed in a more complex geometry. Wurster fluid bed is used for coating and granulation of particles and is composed of two main parts: down bed and up bed. The down bed is a near cylindrical bed with a draft tube in the middle. The up bed is composed of an expanding cone followed by a cylinder. The expanded part causes a reduction in the vertical velocity of particles due to a rapid reduction of gas velocity. Dimensions of the bed were chosen based on Glatt® GPCG 3/5, Wurster 7 equipment. The total volume of the bed was 110 L. and the diameters of the bed in bottom and top sections were 14 and 44 cm, respectively. A draft tube with the length of 30 cm and diameter of 7 cm was placed 2 cm above the distributor plate. More details of the Wurster bed are shown in Fig. 10. The bed was filled with 1 kg of 3-mm pellets with the density of 1500 kg/m^3. This required about 47,200 particles in the simulation. Other simulation conditions and physical properties are listed in Table 3. The physical properties related to contact force are based on the Cellets® pellets [56]. Mean and maximum Courant numbers were 0.26 and 1.02 in this simulation, respectively.

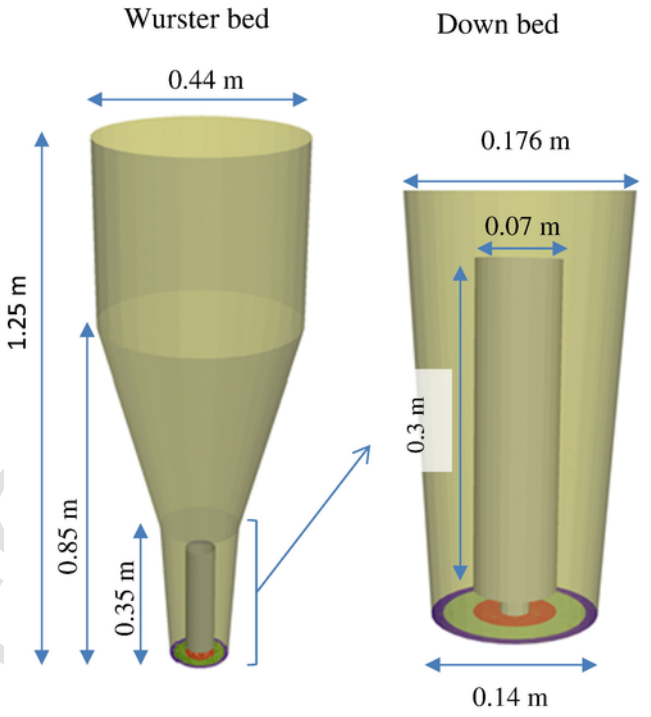

Fig. 10. Dimensions of the Wurster bed.

Table 3
Physical properties and simulation conditions for Wurster fluid bed.

Parameter	Value	Parameter	Value
Particles[a]		Bed	
Size (μm)	3000	Volume (m^3)	0.110
Density (kg/m^3)	1500	Draft tube length/diameter (m)	0.3/0.07
Young modulus (MPa)	10	Young modulus (MPa)	10
Poisson's ratio (−)	0.23	Poisson's ratio (−)	0.23
Dynamic friction (−)	0.23	Dynamic friction (−)	0.23
Rolling friction (−)	0.05	Rolling friction (−)	0.05
Coefficient of restitution (−)	0.65	Coefficient of restitution (−)	0.65
Air		Simulation	
Density (kg/m^3)	1.2	Time step for fluid (s)	1×10^{-4}
Viscosity (Pa·s)	1.8×10^{-5}	Time step for particle (s)	5×10^{-6}
		No. of particles (−)	47,200
		No. of CFD cells (−)	42,000
		Mesh shape (−)	hex
		Mean Courant number (−)	0.26
		Max Courant number (−)	1.02
		Simulation duration (s)	120

[a] Physical properties of the particles are based on the Cellets® pellets reported in [56].

The computational resources were a CPU core and a GPU. It took 30 min to complete each second of the simulation and it was continued for 120 s.

Snapshots of the whole bed and the down bed (cut in half to make inside visible) are shown in Fig. 11a-c. Particles are colored based on their velocity magnitude. The gas velocity trough the distributor plate entering in the draft tube is 11.5 m/s (11U_{mf}) and in the annulus region is 4.5 m/s (4.2 U_{mf}). This is called the velocity profile #1 hereafter. The high gas velocity under the draft tube accelerates particles and produces an upward flow of the particles in it. At the top of the draft tube (in the expansion zone), the gas velocity decreases and results in the deceleration of particles and formation of the fountain. Particles then return back to the bottom of the bed in the annulus region. Since the velocity of the gas entering the annulus region is higher than the minimum fluidization velocity of particles, particles are fluidized at the bubbling regime in that region. Snapshots of this simulation show the bubbling regime characteristics in the annulus. In the draft tube, the slugging conveying occurs. This conveying regime occurs due to formation of bubbles in the space between the distributor plate and draft tube (shown with circles in the figure). These bubbles act as an obstacle against the continuous flow of particles entering the draft tube and disrupt the particle flow (Fig. 11c). When there is no bubble in this space, a continuous flow of particles enters the draft tube as can be seen in Fig. 11b. In addition, in this condition, most of the gas passing through the central jet enters the draft tube due to existence of particles in this space. However, when there is a bubble in this space, a portion of the gas passing through the central jet leaks into the annulus region and the gas velocity decreases in the draft tube. The pulsation in the particle flow entering the draft tube and fluctuations of the gas velocity in the draft tube result in developing a slugging conveying regime. Therefore, an unstable fountain whose maximum height fluctuates during the bed operation is formed in the bed (this was observed by reviewing the animation of this simulation).

To support our statements about the gas leakage into the annulus region, contours of gas velocity in the bed are studied. Fig. 12a shows these gas velocity contours on a plane crossing the center of the bed at time 60.4 s. This corresponds to the snapshot of the bed shown in Fig. 11b. It can be seen that most of the central jet enters the draft tube and forms a stable jet. Fig. 12b shows the gas velocity contour of the bed at time 60.8 s which corresponds to the snapshot of the bed shown in Fig. 11c. This figure shows that when bubbles exist in the space between the distributor and the draft tube, the gas leaks into the annulus region and the gas velocity in the draft tube decreases.

In the next simulation, the gas velocity passing through the distributor under the draft tube (central jet) was increased to 14 m/s (13.5 U_{mf}) and the gas velocity under the annulus region was reduced to 1 m/s (0.95 U_{mf}). This is called velocity profile #2 hereafter. A snapshot of the whole bed and some snapshots of the down bed (cut in half to make inside visible) are shown in Fig. 13. Particles are colored based on their velocity magnitude in this figure. A stable fountain is formed in the bed that rises up to 0.85 m. As can be seen in Fig. 13b&c, a fixed bed is formed in the annulus region and a dispersed conveying regime is formed in the draft tube. A continuous flow of particles is formed from annulus to draft tube due to the absence of bubbles in the annulus.

The portability and scalability of the code is another important aspect. The code is portable and it can be executed on every PC that is equipped with a CUDA-enabled GPU. We tested this code on a number of PCs ranging from laptop to desktop computers. However, the scalability of the code is limited by the available memory in GPU. Since each GPU has its dedicated memory and this memory cannot be extended, the scale of the problem (number of particles) depends on the size of this memory. For example, in the PC used in the current study, the CPU side (host side) had access to 12 GB memory while the GPU side (device side) had access to 2 GB of memory. This problem can be mitigated by using multiple GPUs or using newer GPUs with larger memories.

5. Conclusion

This study concerns the important details of implementation of an efficient hybrid CFD-DEM solver and its performance in predicting the hydrodynamics of gas-solid flows in bubbling fluidized beds and spouted beds. It was tried to develop the new solver in a way that it supports complex container/wall geometries, supports various shapes of the mesh, converges at very high local and global fluid velocities (high Courant numbers) and uses the maximum computational resources available on an ordinary computer to obtain the best execution performance. Governing equations of fluid phase were solved by the open source CFD package, OpenFOAM®, executed on multiple CPU processors using MPI. The solver for DEM equations was implemented in parallel using the CUDA® platform. The entire calculations were parallelized and executed on a GPU. In addition, computa-

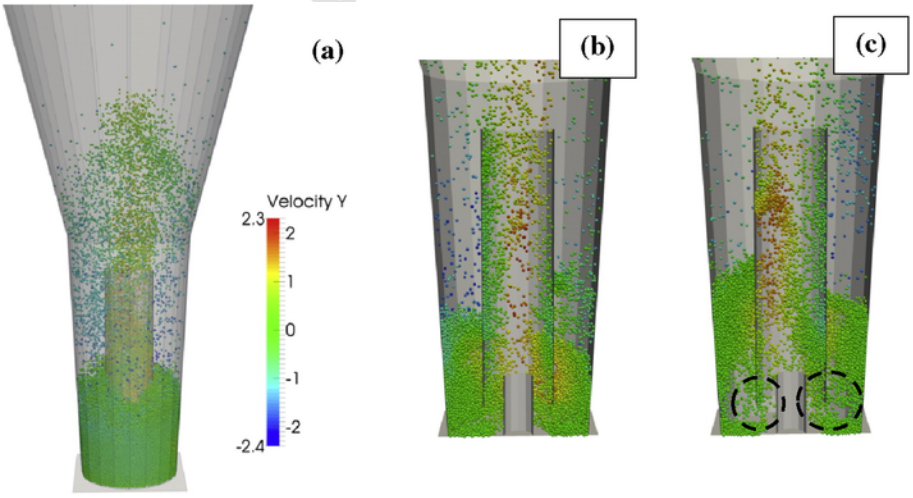

Fig. 11. (a) A Snapshot of the Wurster bed (with velocity profile #1) and snapshot of the particles in the down bed part of the Wurster at times (b) 60.4 s and (c) 60.8 s. Particles are colored based on their velocity magnitude and the snapshots of the down bed are half-cut to make the inside of the bed visible.

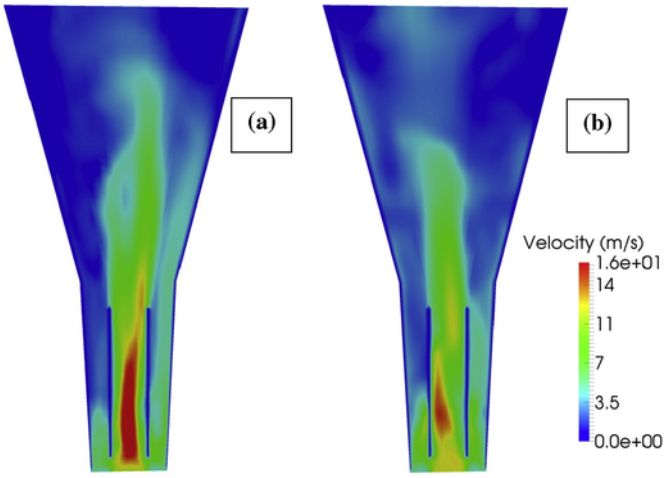

Fig. 12. Contour of the gas velocity in the Wurster bed with velocity profile #1 at times (a) 60.4 s and (b) 60.8 s.

tions related to the calculation of coupling parameters were also parallelized using MPI.

The solver was first verified by very simple granular and coupled problems whose analytical solutions exist. Among the three main components of the solver, CFD solver, DEM solver and coupling solver, only the latter two were examined. The results showed that the solver can regenerate the exact solution of the examined granular and coupled problems with acceptable errors. The solver was then evaluated in three gas-solid flows with various geometries (from simple to complex) and different number of particles. The solver was executed on a desktop computer equipped with a 4-core CPU with 3.6 GHz frequency and a NVIDIA GeForce® 660Ti GPU. For a large system that contains of 870 k particles, it took about 6 h (with two CPU cores) to complete each second of simulation while in a smaller system with 47 k particles, this took only 30 min (with one CPU core). Results of the new solver were compared with the experimental data. It was shown that the solver can predict the frequency of bubbles and the intensity/share of macro structures in the bubbling regime, while underestimates the intensity/share of meso-structures. The solver can also predict the hydrodynamics of a spouted bed with draft tube in terms of shape and maximum height of fountain, particle concentration profile in different parts and time-averaged upward velocity of particles. The solver was also used to investigate the particle dynamics in a Wurster bed. Two velocity profiles were tested. In the first velocity profile (gas velocity greater than U_{mf} in annulus region) an unstable fountain with the slugging conveying in the draft tube was observed while in the second velocity profile (gas velocity near the U_{mf} in annulus region), a stable fountain with dispersed conveying regime in draft tube. This was found to be attributed to the formation of the bubbles in the annulus region.

This solver is under more developments to solve mass and energy equations for both phases and perform interphase mass and energy coupling. Moreover, a new parallel solver (on GPU) will be developed for discrete modeling of a spraying system. This solver then will be coupled to the existing solver through mass, energy and momentum couplings.

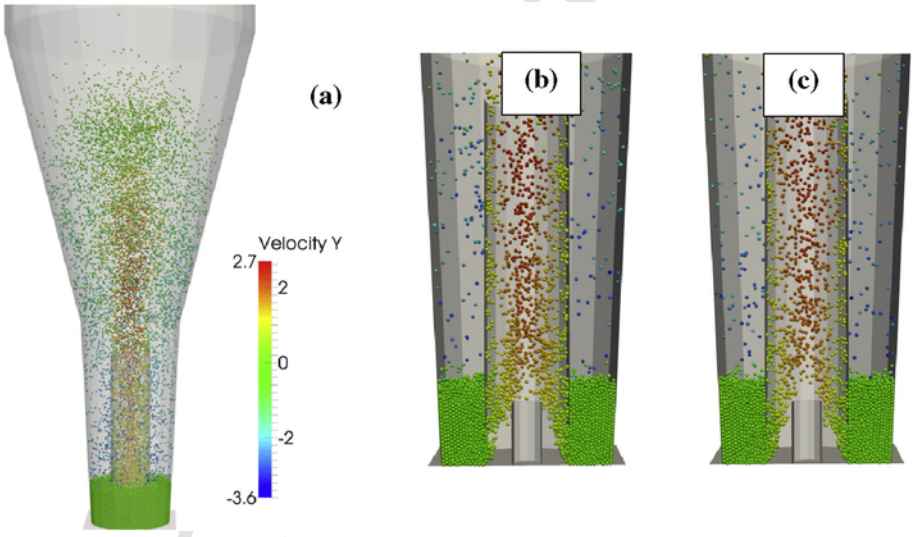

Fig. 13. (a) A Snapshot of the Wurster bed (with velocity profile #2) and snapshot of the particles in the down bed part of the Wurster at times (b) 60 s and (c) 60.2 s. Particles are colored based on their velocity magnitude and the snapshots of the down bed are half-cut to make the inside of the bed visible.

References

[1] Y. Tsuji, Multi-scale modeling of dense phase gas–particle flow, Chem. Eng. Sci. 62 (2007) 3410–3418.
[2] Q.J. Zheng, Z.Y. Zhou, A.B. Yu, Contact forces between viscoelastic ellipsoidal particles, Powder Technol. 248 (2013) 25–33.
[3] L. Vu-Quoc, X. Zhang, An elastoplastic contact force-displacement model in the normal force–displacement model in the normal direction: displacement-driven version, Proc. Math. Phys. Eng. Sci. 455 (1999) 4013–4044.
[4] Q.J. Zheng, H.P. Zhu, A.B. Yu, Finite element analysis of the contact forces between a viscoelastic sphere and rigid plane, Powder Technol. 226 (2012) 130–142.
[5] H. Kruggel-Emden, F. Stepanek, A. Munjiza, A study on adjusted contact force laws for accelerated large scale discrete element simulations, Particuology 8 (2010) 161–175.
[6] F.P. Di Maio, A. Di Renzo, Analytical solution for the problem of frictional-elastic collisions of spherical particles using the linear model, Chem. Eng. Sci. 59 (2004) 3461–3475.
[7] A. Di Renzo, F.P. Di Maio, An improved integral non-linear model for the contact of particles in distinct element simulations, Chem. Eng. Sci. 60 (2005) 1303–1312.
[8] S. Benyahia, M. Syamlal, T.J. O'Brien, Extension of Hill-Koch-Ladd drag correlation overall ranges of Reynolds number and solids volume fraction, Powder Technol. 162 (2006) 166–174.
[9] R.J. Hill, D.L. Koch, J.C. Ladd, The first effects of fluid inertia on flows in ordered and random arrays of spheres, J. Fluid Mech. 448 (2001) 213–241.
[10] R.J. Hill, D.L. Koch, J.C. Ladd, Moderate-Reynolds-numbers flows in ordered and random arrays of spheres, J. Fluid Mech. 448 (2001) 243–278.
[11] R. Beetstra, M.A. van der Hoef, J.A.M. Kuipers, Drag force of intermediate Reynolds number flow past mono- and bidisperse arrays of spheres, AICHE J. 53 (2007) 489–501.
[12] M.A. van der Hoef, R. Beetstra, J.A.M. Kuipers, Lattice Boltzmann simulations of low Reynolds number flow past mono- and bidisperse arrays of spheres: results for the permeability and drag force, J. Fluid Mech. 528 (2005) 233–254.
[13] F. Cello, A. Di Renzo, F.P. Di Maio, A semi-empirical model for the drag force and fluid–particle interaction in polydisperse suspensions, Chem. Eng. Sci. 65 (2010) 3128–3139.
[14] N.S. Cheng, Comparison of formulas for drag coefficient and settling velocity of spherical particles, Powder Technol. 189 (2009) 395–398.
[15] R. Di Felice, The voidage function for fluid–particle interaction systems, Int. J. Multiphase Flow 20 (1994) 153–159.
[16] Y.Q. Feng, A.B. Yu, Assessment of model formulations in the discrete particle simulation of gas-solid flow, Ind. Eng. Chem. Res. 43 (2004) 8378–8390.
[17] Z.Y. Zhou, S.B. Kuang, K.W. Chu, A.B. Yu, Discrete particle simulation of particle-fluid flow: model formulations and their applicability, J. Fluid Mech. 661 (2010) 482–510.
[18] Z. Mansourpour, N. Mostoufi, R. Sotudeh-Gharebagh, A mechanistic study of agglomeration in fluidised beds at elevated pressures, Can. J. Chem. Eng. 91 (2013) 560–569.
[19] Z. Mansourpour, H.R. Norouzi, N. Mostoufi, R. Sotudeh-Gharebagh, Numerical hydrodynamic investigation of agglomerating fluidized bed, In: 10th China-Japan SymposiumTokyo, Japan, 2010.
[20] M.A. Hassani, R. Zarghami, H.R. Norouzi, N. Mostoufi, Numerical investigation of effect of electrostatic forces on the hydrodynamics of gas-solid fluidized beds, Powder Technol. 246 (2013) 16–25.
[21] T. Mikami, H. Kamiya, M. Horio, Numerical simulation of cohesive powder behavior in a fluidized bed, Chem. Eng. Sci. 53 (1998) 1927–1940.
[22] S. Karimi, Z. Mansourpour, N. Mostoufi, R. Sotudeh-Gharebagh, CFD-DEM study of temperature and concentration distribution in a polyethylene fluidized bed reactor, Part. Sci. Technol. 29 (2011) 163–178.
[23] H. Zhou, G. Flamant, D. Gauthier, DEM-LES simulation of coal combustion in a bubbling fluidized bed. Part II: coal combustion at the particle level, Chem. Eng. Sci. 59 (2004) 4205–4215.
[24] D. Liu, X. Chen, W. Zhou, C. Zhao, Simulation of char and propane combustion in a fluidized bed by extending DEM–CFD approach, Proc. Combust. Inst. 33 (2011) 2701–2708.
[25] F.P. Di Maio, A. Di Renzo, D. Trevisan, Comparison of heat transfer models in DEM-CFD simulations of fluidized beds with an immersed probe, Powder Technol. 193 (2009) 257–265.
[26] Z.Y. Zhou, A.B. Yu, P. Zulli, A new computational method for studying heat transfer in fluid bed reactors, Powder Technol. 197 (2010) 102–110.
[27] K.F. Malone, B.H. Xu, Particle-scale simulation of heat transfer in liquid-fluidised beds, Powder Technol. 184 (2008) 189–204.
[28] H.R. Norouzi, R. Zarghami, R. Sotudeh-Gharebagh, N. Mostoufi, Coupled CFD-DEM Modeling: Formulation, Implementation and Application to Multiphase Flows, Wiley, 2016.
[29] Z.Y. Zhou, A.B. Yu, P. Zulli, Particle scale study of heat transfer in packed and bubbling fluidized beds, AICHE J. 55 (2009) 868–884.
[30] Y. Tsuji, T. Tanaka, T. Ishida, Lagrangian numerical simulation of plug flow of cohesionless particles in a horizontal pipe, Powder Technol. 71 (1992) 239–250.
[31] Y.C. Zhou, B.D. Wright, R.Y. Yang, B.H. Xu, A.B. Yu, Rolling friction in the dynamic simulation of sandpile formation, Phys. A 269 (1999) 536–553.
[32] S. Ergun, Fluid flow through packed columns, Chem. Eng. Prog. 48 (1952) 89–94.
[33] C.Y. Wen, Y.H. Yu, Mechanics of fluidization, Chem. Eng. Prog. Symp. Ser. 62 (1966) 100–111.
[34] D. Gidaspow, Multiphase Flow and Fluidization: Continuum and Kinetic Theory Description, Academic Press, San Diego, 1994.
[35] H. Mazhar, T. Heyn, D. Negrut, A scalable parallel method for large collision detection problems, Multibody Syst. Dyn. 26 (2011) 37–55.
[36] C. Ericson, Real-Time Collision Detection, Elsevier, USA, 2005.
[37] H. Kruggel-Emden, M. Sturm, S. Wirtz, V. Scherer, Selection of an appropriate time integration scheme for the discrete element method (DEM), Comput. Chem. Eng. 32 (2008) 2263–2279.
[38] H.G. Weller, G. Tabor, H. Jasak, C. Fureby, A tensorial approach to computational continuum mechanics using object-oriented techniques, Comput. Phys. 12 (1998) 620–631.
[39] H. Jasak, Error Analysis and Estimation for the Finite Volume Method with Applications to Fluid Flows, Department of Mechanical Engineering, Imperial College of Science, Technology and Medicine, 1996.
[40] H.R. Norouzi, Modeling of Pharmaceutical Particle Coating Process Using Discrete Element Method, Department of Chemical Engineering, University of Tehran, 2016.
[41] S.V. Patankar, Numerical Heat Transfer and Fluid Flow, Hemisphere Publishing Corporation, 1980.
[42] R.I. Issa, Solution of the implicitly discretised fluid flow equations by operator-splitting, J. Comput. Phys. 62 (1986) 40–65.
[43] J.E. Hilton, L.R. Mason, P.W. Cleary, Dynamics of gas–solid fluidised beds with non-spherical particle geometry, Chem. Eng. Sci. 65 (2010) 1584–1596.
[44] B.P.B. Hoomans, J.A.M. Kuipers, W.J. Briels, W.P.M.v. Swaaij, Discrete particle simulation of bubble and slug formation in a two-dimensional gas-fluidised bed: a hard-sphere approach, Chem. Eng. Sci. 51 (1996) 99–118.
[45] R.W. Erney, Verification and Validation of Single Phase and Cavitating Flows Using an Open Source CFD Tool, Pennsylvania State University, 2008.
[46] R. Garg, J. Galvin, T. Li, S. Pannala, Open-source MFIX-DEM software for gas–solids flows: part I—verification studies, Powder Technol. 220 (2012) 122–137.
[47] L. Schiller, A. Nauman, A drag coefficient correlation, VDI Zeitung 77 (1935) 318.
[48] H.R. Norouzi, M. Tahmasebpoor, R. Zarghami, N. Mostoufi, Multi-scale analysis of flow structures in fluidized beds with immersed tubes, Particuology 21 (2015) 99–106.
[49] H.R. Norouzi, B. Haddadi-Sisakht, H. Azizpour, R. Zarghami, R. Sotudeh-Gharebagh, N. Mostoufi, Wall vibration for characterizing fluidization hydrodynamics, Can. J. Chem. Eng. 92 (2014) 1783–1790.
[50] J.R. van Ommen, S. Sasic, J. Van der Schaaf, S. Gheorghiu, F. Johnsson, M.-O. Coppens, Time-series analysis of pressure fluctuations in gas–solid fluidized beds—a review, Int. J. Multiphase Flow 37 (2011) 403–428.
[51] R. Zarghami, N. Mostoufi, R. Sotudeh-Gharebagh, Nonlinear characterization of pressure fluctuations in fluidized beds, Ind. Eng. Chem. Res. 47 (2008) 9497–9507.
[52] D.H. Gracias, G.A. Somorjai, Continuum force microscopy study of the elastic modulus, hardness and friction of polyethylene and polypropylene surfaces, Macromolecules 31 (1998) 1269–1276.
[53] A. Tamburini, A. Cipollina, G. Micale, A. Brucato, M. Ciofalo, CFD simulations of dense solid–liquid suspensions in baffled stirred tanks: prediction of suspension curves, Chem. Eng. J. 178 (2011) 324–341.
[54] A. Tamburini, A. Cipollina, G. Micale, A. Brucato, M. Ciofalo, Influence of drag and turbulence modelling on CFD predictions of solid liquid suspensions in stirred vessels, Chem. Eng. Res. Des., 92 1045–1063.
[55] V.S. Sutkar, N.G. Deen, B. Mohan, V. Salikov, S. Antonyuk, S. Heinrich, J.A.M. Kuipers, Numerical investigations of a pseudo-2D spout fluidized bed with draft plates using a scaled discrete particle model, Chem. Eng. Sci. 104 (2013) 790–807.
[56] R. Šibanc, T. Kitak, B. Govedarica, S. Srčič, R. Dreu, Physical properties of pharmaceutical pellets, Chem. Eng. Sci. 86 (2013) 50–60.
[57] S. Antonyuk, S. Heinrich, N. Deen, H. Kuipers, Influence of liquid layers on energy absorption during particle impact, Particuology 7 (2009) 245–259.